Gottschalk, M. (2019): An EOS for the Lennard-Jones fluid: A virial expansion approach. - *AIP Advances*, *9*.

DOI: http://doi.org/10.1063/1.5119761

An EOS for the Lennard-Jones fluid: A virial expansion approach

Cite as: AIP Advances **9**, 125206 (2019); https://doi.org/10.1063/1.5119761
Submitted: 12 July 2019 . Accepted: 31 October 2019 . Published Online: 04 December 2019

Matthias Gottschalk

An EOS for the Lennard-Jones fluid: A virial expansion approach

Cite as: AIP Advances 9, 125206 (2019); doi: 10.1063/1.5119761
Submitted: 12 July 2019 • Accepted: 31 October 2019 •
Published Online: 4 December 2019

Matthias Gottschalk[a]

AFFILIATIONS

GFZ German Research Centre for Geosciences, Section 3.6: Chemistry and Physics of Earth Materials, 14473 Potsdam, Telegrafenberg, Germany

[a]Electronic addresses: gottschalk@gfz-potsdam.de and mcgottschalk@me.com

ABSTRACT

A large number (>30 000) of *Monte Carlo* simulations in range of 0.002–1.41 ρ^* and $T^* \leq 25$ (* for reduced, dimensionless) was performed, producing a dense grid of state points for the internal energy U^* and pressure p^*. The dense grid in ρ^* allows the direct integration to obtain the *Helmholtz free energy* F^*. The results in U^*, p^*, and F^* were used to fit an *equations of state (EOS)* for the *Lennard-Jones* fluid using the virial thermal coefficients B_2–B_6 taken from the literature and additional empirical coefficients (C_7-C_{16}), which correct the errors due to nonconverging behavior of virial thermal coefficients. Those additional coefficients have the same mathematical form as the virial thermal coefficients. The *EOS* allows an extrapolation to extreme conditions above $T^* > 100$ and $\rho^* > 2$.

I. INTRODUCTION

For chemical equilibrium calculations within the Earth, the thermodynamic properties of pure fluids and their mixtures up to very high temperatures T and pressures p are required. Considering conditions in the lower crust or upper mantle of the Earth, thermodynamic properties of species at pressures and temperatures above 2 GPa and 1000 K have to be evaluated. Within gas planets, conditions are even more extreme. However, very few experimental p-T data for volumes V exist for pure fluids at these extreme conditions. For fluid mixtures, they are practically not existent. Therefore, theoretically derived *equations of state (EOS)* are a viable choice for the prediction of the required fugacities for equilibrium calculations of chemical species as a function of T and p. In addition, the speciation in a fluid, for example, the occurrence of H_2O or H_4O_2 in water, will be a key point in the future development to enhance the chemical understanding of equilibrium processes. For thermodynamic equilibrium calculations, the properties of species are required and the chemical compound (e.g., H_2O) must be understood as a mixture of their species. This will be important for solubility calculations, for which speciation is essential.

One choice of an *EOS* to predict fugacities of any chemical species in mixtures as a function of p and T is based on the perturbation theory. A simple perturbation *EOS*, as given by Churakov and Gottschalk,[1,2] is quite successful in predicting the properties in such fluid mixtures. However, this *EOS*[1,2] is restricted in the number of implemented molecular interaction types and suffers from numerical instability at high p, rendering it difficult to extrapolate to extreme conditions. Therefore, efforts are underway to further investigate the potential of perturbation theory to formulate an *EOS*, which is applicable to geologically relevant conditions.

The *Helmholtz free energy* F and its derivatives with respect to density ρ and temperature T describe all relevant thermodynamic properties. Perturbation theory uses the ideal gas F^o as a starting point and adds a residual part F^r, which is formulated using a well-known model as a reference F^r_{ref}. Expanding F^r in λ, a dimensionless parameter that can take on values ranging continuously from 0 (no perturbation) to 1 (the full perturbation) and hereby considering two- and many-body interactions accounting for multipole, induction, dispersion, as well as repulsion forces of nonspherical molecules,[3–8] F becomes

$$F = F^o + F^r = F^o + F^r_{\text{ref}} + F^\lambda + F^{\lambda\lambda} + F^{\lambda\lambda\lambda} + \cdots. \quad (1)$$

This communication deals with the F^r_{ref} term of Eq. (1). The reference model chosen here is based on the *12-6 Lennard-Jones* (*LJ*)

potential[9]

$$u_{\mathrm{LJ}} = 4\,\varepsilon\left[\left(\frac{\sigma}{r}\right)^{12} - \left(\frac{\sigma}{r}\right)^{6}\right], \tag{2}$$

where σ is the finite distance at which the interparticle potential is zero, ε is the depth of the potential well, and r is the distance between two particles. The *12-6 Lennard-Jones* is a special form of the *Mie* potential[10]

$$u_{\mathrm{Mie}} = \left(\frac{n}{n-m}\right)\left(\frac{n}{m}\right)^{m/(n-m)}\left[\left(\frac{\sigma}{r}\right)^{n} - \left(\frac{\sigma}{r}\right)^{m}\right], \tag{3}$$

where n and m are adjustable coefficients 12 and 6 for the *LJ* potential.

The restriction to two parameters σ and ε in the *LJ* potential allows the exploration of states with reduced, dimensionless variables (e.g., ρ^*, T^*, and p^*) resulting in dimensionless fluid properties without addressing σ and ε explicitly:

$$T^* = \frac{k_B T}{\varepsilon}, \quad \rho^* = \rho\sigma^3, \quad p^* = \frac{\rho\sigma^3}{\varepsilon}, \tag{4}$$

with

$$\rho = v^{-1} = N/V, \tag{5}$$

where k_B is the *Boltzmann* constant, T the temperature, and ρ the number density, while the * designates their reduced, dimensionless form. Exploration of states is then usually done for ρ^* and T^*.

A number of *EOS* are available for the *LJ* fluid,[11–17] which all have their merits. The reasons to formulate another, new *EOS* are as follows:

- the new *EOS* should cover the ρ^*–T^* comprehensive space for which simulation data are derived here ($0.002 \le \rho^* \le 1.41$, $T^* \le 25$);
- should allow extrapolation to extreme conditions ($\rho^* > 2$, $T^* > 100$);
- should be based on a dense array of state points;
- should also be based on a large set of F^* values obtained by integration over ρ^*, without the need of particle insertion in *Monte Carlo (MC)* simulations;
- the pair and triplet correlation functions over the total phase space should be available and are therefore calculated because their integrals over distance and orientation are needed in perturbation theory.

The presentation of the correlation functions and their integrals will be subject to a further communication.

In this context, a large number of *Monte Carlo* simulations (>30 000) in the canonical *NVT* ensemble were performed and used as input for a formulation of an *EOS*.

The thermodynamic formalism for the derivation of the *EOS* follows the outline of Thol *et al.*[17] with only minor changes to the procedure itself.[18–22] However, the mathematical functional form of the *EOS* is quite different from that of Thol *et al.*[17]

The *EOS* is written in terms of the reduced, dimensionless *Helmholtz free energy* a^* as a function of the inverse reduced temperature T^* and density ρ^*, where a^* is divided into two terms indicating an ideal-gas (superscript o) and a residual part

TABLE I. Reduced, dimensionless thermodynamic properties based on the definition of Eq. (8).

Properties
Pressure and its derivatives
$p^* = -\left(\frac{\partial a^*}{\partial v^*}\right)_T = \rho^* T^* (A_{01}^o + A_{01}^r) = \rho^* T^* (1 + A_{01}^r)$
$\left(\frac{\partial p^*}{\partial \rho^*}\right)_T = T^* (1 + 2A_{01}^r + A_{02}^r)$
$\left(\frac{\partial^2 p^*}{\partial \rho^{*2}}\right)_T = \frac{T^*}{\rho^*}(2A_{01}^r + 4A_{02}^r + A_{03}^r)$
$\left(\frac{\partial p^*}{\partial T^*}\right)_\rho = \rho^* (1 + A_{01}^r - A_{11}^r)$
$\left(\frac{\partial p^*}{\partial v^*}\right)_T = -\rho^{*2}\left(\frac{\partial p^*}{\partial \rho^*}\right)_T = -\rho^{*2} T^* (1 + 2A_{01}^r + A_{02}^r)$
$\left(\frac{\partial^2 p^*}{\partial v^{*2}}\right)_T = 2\rho^{*3}\left(\frac{\partial p^*}{\partial \rho^*}\right)_T + \rho^{*4}\left(\frac{\partial^2 p^*}{\partial \rho^{*2}}\right)_T = \rho^{*3} T^* (2 + 6A_{01}^r + 6A_{02}^r + A_{03}^r)$
Entropy
$s^* = -\left(\frac{\partial a^*}{\partial T^*}\right)_v = A_{10}^o + A_{10}^r - A_{00}^o - A_{00}^r$
Internal energy
$u^* = a^* + T^* s^* = T^* (A_{10}^o + A_{10}^r)$
Enthalpy
$h^* = u^* + p^* v^* = T^* (1 + A_{10}^o + A_{10}^r + A_{01}^r)$
Gibbs free energy
$g^* = \left(\frac{\partial h^*}{\partial T^*}\right)_p = T^* (1 + A_{00}^o + A_{00}^r + A_{01}^r)$
Isochoric heat capacity
$c_v^* = \left(\frac{\partial u^*}{\partial T^*}\right)_v = -(A_{20}^o + A_{20}^r)$
Isobaric heat capacity
$c_p^* = \left(\frac{\partial h^*}{\partial T^*}\right)_p = c_v^* + \frac{T^* \alpha^2}{\rho^* \beta_T^*} = -(A_{20}^o + A_{20}^r) + \frac{(1 + A_{20}^r - A_{11}^r)^2}{1 + 2A_{01}^r + A_{02}^r}$
Compressibility factor
$Z = 1 + A_{01}^r$
Fugacity coefficient
$\phi = e^{A_{00}^r + A_{01}^r}/(1 + A_{01}^r)$
*n*th *thermal virial coefficient* ($n \ge 2$)
$B_n = \frac{1}{(n-2)!} \lim_{\rho \to 0}\left(\frac{1}{\rho^{*n-1}} \frac{\partial^{n-1} A_{00}^r}{\partial \rho^{*n-1}}\right)_T$
Speed of sound
$w^* = \sqrt{\left(\frac{\partial p^*}{\partial \rho^*}\right)_s} = \sqrt{T^*\left(1 + 2A_{01}^r + A_{02}^r - \frac{(1 + A_{01}^r - A_{11}^r)^2}{A_{20}^0 + A_{20}^r}\right)}$
Grüneisen coefficient
$\Gamma^* = \frac{\left(\frac{\partial p^*}{\partial T^*}\right)_\rho}{\rho^* c_v^*} = -\frac{1 + A_{01}^r - A_{11}^r}{(A_{20}^0 + A_{20}^r)}$
Isothermal compressibility
$\beta_T^* = \frac{1}{\rho^*\left(\frac{\partial p^*}{\partial \rho^*}\right)_T} = \frac{1}{\rho^* T^* (1 + 2A_{01}^r + A_{02}^r)}$
Thermal pressure coefficient
$\gamma^* = \left(\frac{\partial p^*}{\partial T^*}\right)_\rho = \rho^* (1 + A_{01}^r - A_{11}^r)$
Thermal expansion coefficient
$\alpha^* = \beta_T^* \gamma^* = \frac{\left(\frac{\partial p^*}{\partial T^*}\right)_\rho}{\rho^*\left(\frac{\partial p^*}{\partial \rho^*}\right)_T} = \frac{(1 + A_{01}^r - A_{11}^r)}{T^* (1 + 2A_{01}^r + A_{02}^r)}$

(superscript r):

$$a^*(\tau,\delta) = \frac{a^o(T,\rho) + a^r(T,\rho)}{k_B T} = a^{o*}(\tau,\delta) + a^{r*}(\tau,\delta), \quad (6)$$

with $a = F/N$ the *Helmholtz free energy* per particle. Additionally, τ and δ are defined as

$$\tau = \frac{1}{T^*}, \quad \delta = \rho^*. \quad (7)$$

In contrast to Thol *et al.*,[17] these definitions do not include the critical properties T_c^* and ρ_c^*. They are not a prerequisite for the derivation of the presented *EOS*. ρ^* is sometimes renamed to δ to be in agreement with Thol *et al.*,[17] but this is used here loosely.

All thermodynamic properties can be calculated from Eq. (6) and its derivatives with respect to τ and δ. A selection is listed in Table I. For the respective derivatives as in Thol *et al.*,[17] the following notation is used:

$$A_{mn} = A^o_{mn} + A^r_{mn} = \tau^m \delta^n \frac{\partial^{m+n}(a^{o*} + a^{r*})}{\partial\tau^m \partial\delta^n}. \quad (8)$$

For an ideal gas, a^{o*} is

$$a^{o*} = h_r^{o*}\tau - s_r^{o*} - 1 + \log\frac{\delta\,\tau_r}{\delta_r\,\tau} - \tau\int_{\tau_r}^{\tau}\frac{c_p^{o*}}{\tau^2}d\tau + \int_{\tau_r}^{\tau}\frac{c_p^{o*}}{\tau}d\tau, \quad (9)$$

where h_r^{o*} and s_r^{o*} are the reduced, dimensionless enthalpy and entropy at reference conditions (subscript r) in their standard state and c_p^{o*} the heat capacity at constant pressure at standard state conditions. The standard state refers to a hypothetical ideal gas at p_r^*. Values of h_r^{o*}, s_r^{o*}, as well as c_p^{o*} as functions of T^* can be found for each ideal gas in thermodynamic reference tables. In Eq. (9), the fourth term on the right hand side can be replaced by

$$\log\frac{\delta\,\tau_r}{\delta_r\,\tau} = \log\frac{p^*}{p_r^*}. \quad (10)$$

For a classical monoatomic gas, the isobaric heat capacity is $c_p^{o*} = 2.5$. Therefore, integration of (9) yields

$$a^{o*} = \ln\delta + \frac{3}{2}\ln\tau + c_1\tau + c_2, \quad (11)$$

with

$$c_1 = h_r^{o*} - \frac{5}{2\tau_r} \quad (12)$$

and

$$c_2 = \frac{3}{2} - s_r^{o*} + \frac{3}{2}\ln\tau_r - \ln\delta_r. \quad (13)$$

II. MONTE CARLO SIMULATIONS

Using the program *mc_nvt_lj* by Allen and Tildesley[23] (code is available at http://github.com/Allen-Tildesley), *Monte Carlo* (*MC*) simulations in the *NVT* ensemble were performed. A total of 32 705 simulations were run providing a dense array of state points. The conditions of this set of simulations are given in Table II. This set covers all possible phases: gas, fluid, and solid. In the *MC* simulations, the following resulting configurations are distinguished according to their result:

- stable: outside vapor/fluid field, 1 phase in the simulation, homogeneous δ in the box;
- metastable: within the vapor/fluid field, but *MC* shows only 1 phase in the simulation, homogeneous δ in the box;
- heterogeneous: within the vapor/fluid field, but *MC* shows 2 phases in the simulation, heterogeneous δ in the box.

TABLE II. Conditions of the *MC* simulations.

T^*_{from}	T^*_{to}	ΔT^*	ρ^*_{from}	ρ^*_{to}	$\Delta\rho^*$	n
0.05	2.95	0.05	0.01	1.41	0.01	8 319
0.05	1.00	0.05	0.002	0.009	0.001	160
3.0	18.0	0.1	0.01	1.41	0.01	21 291
18.5	25.0	0.5	0.01	1.41	0.01	1 974
1.305	1.335	0.001	0.300	0.330	0.001	961

At each state point, 1372 *LJ* particles were equilibrated using 5×10^4 cycles and subsequently sampled for 0.75×10^6 cycles. One cycle consists of 1372 trial moves, one for each particle. Besides the final result, the output of the program provides additional information after completion of a certain amount of cycles, so-called blocks. Each block reports the move acceptance ratio, U^*, p^*, and the configuration temperature T^*_{config} as well as stores the its respective configurational of particles. T^*_{config} can be used as a diagnostic tool for the simulation run.[23] The stored configurations can be used afterward to calculate pair and triplet correlations functions. For thermodynamic sampling, the block size was 1000 cycles. Standard errors of the mean σ_M for U^* and p^* were calculated using the block output for U^* and p^*.

The move acceptance ratio was varied automatically by the program *mc_nvt_lj* (see Ref. 23, p. 159).

The program *mc_nvt_lj*, using long-range corrections, provides the *internal energy* U^* and *pressure* p^* from which A^r_{10} and A^r_{01} can be calculated using Eq. (8) (see also Table I).

Batches of simulations were performed in T^*-increments of 0.05 or 0.1, starting with the final output of the previous configuration. The first configuration of a batch was a *fcc*-lattice. For densities $\rho^* \le 1.37$, a cutoff of 5.0 was used, and for $\rho^* > 1.37$, a cutoff of 4.5 was used. The selection of the cutoff was intended to be a compromise between accuracy and computing cost. For $\rho^* = 1.372$, a cutoff of 5.0 is equal to the half of the box length (L/2).

Table III shows exemplarily the effect of a cutoff of 5.0 vs half of the box length (L/2) as used by Thol *et al.*[17] Here, in total 176 simulations were conducted at identical conditions as in Thol *et al.*[17] For A^r_{01}, except for 1 simulation, the differences between the values in Thol *et al.*[17] and the presented values are within a range of −0.021 to 0.001. For A^r_{10}, except for 3 values, the differences are in range of ±0.01. If the range is narrowed to ±0.005, 12 values are outside this range. So, as a conclusion, the chosen cutoff of 5.0 (4.5 for $\rho^* > 1.37$) and the selected number of cycles seem to be justified.

TABLE III. Comparison of *MC* simulations with a cutoff of 5.0 vs half the box length (L/2) used by Thol *et al.*[17]

		MC (cutoff 5.)		*MC* - Thol *et al.*[17]	
ρ^*	T^*	A_{01}^r	A_{10}^r	A_{01}^r	A_{10}^r
0.01	0.9	−0.063 56(5)	−0.111 11(10)	−0.063 71(4)	−0.111 15(2)
0.85	0.9	0.776 1(8)	−6.580 1(1)	0.762 9(24)	−6.581 9(4)
0.45	1.3	−0.789 2(6)	−2.397 0(5)	−0.802 1(6)	−2.378 2(3)
0.85	1.3	2.243 1(10)	−4.250 1(2)	2.232 1(16)	−4.250 9(3)
0.10	2.0	−0.111 19(11)	−0.333 77(12)	−0.110 92(6)	−0.333 41(2)
1.00	2.0	6.602 6(12)	−2.519 6(2)	6.587 6(20)	−2.522 1(4)
0.10	5.0	0.066 05(10)	−0.102 17(3)	0.065 96(5)	−0.102 01(1)
0.60	5.0	1.314 2(3)	−0.539 36(5)	1.310 1(4)	−0.539 41(6)
1.08	5.0	6.966 5(7)	−0.284 25(15)	6.957 7(12)	−0.285 76(25)

The grid of A_{01}^r values with respect to ρ^* at constant T^* is quite dense; therefore, A_{00}^r can be calculated by numerical integration

$$A_{00}^r = \int_0^{\rho^*} \frac{p^* - T^*\rho^*}{\rho^{*2}} d\rho^* = \frac{1}{\tau} \int_0^{\delta} \frac{A_{01}^r}{\delta} d\delta. \tag{14}$$

However, integration is only possible when the function A_{01}^r is continuously known starting from $\rho^* = 0$. This is only the case for $T^* \geq 1.3$ or for vapor ($\delta^* < 0.3$, $T^* < 1.3$).

The fluid/solid *MC*-separation line, the location above which no fluid simulation data are available, is detected by discontinuities[17] of A_{10}^r and A_{01}^r at constant T^* with respect to ρ^* as illustrated in Fig. 1. In Fig. 1, results to left of the discontinuity are interpreted to belong to the fluid state and to the right to the solid state. This discontinuity simply identifies the location where the solid spontaneously melts during the simulations and such defines the *MC*-separation line.

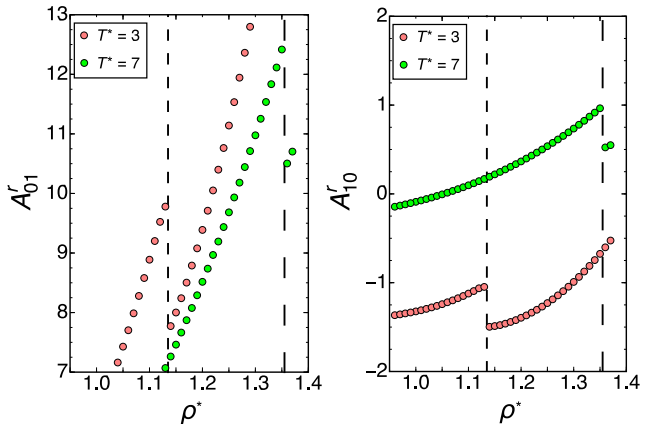

FIG. 1. At constant T^*, A_{01}^r and A_{10}^r show marked discontinuities in respect to ρ^*. Results to left of the dashed line are attributed to the fluid and to the right to the solid state. Short dashed $T^* = 3$ and long dashed $T^* = 7$.

The fluid/solid phase *MC*-separation line ($T^* < 8.6$) is given by the function

$$fs(\delta) = a_1 + a_2\,\delta + a_3\,\delta^2 + a_4\,\delta^3. \tag{15}$$

In the vapor/fluid two phase field, heterogeneous configurations occur, which result in heterogeneities in density within the simulation box and are due to either gas + fluid or gas + solid in the box. Within this region, simulation results must be discarded. The heterogeneous phase region can be approximated by using the following function:

$$h(\delta) = a_1 + a_2\,\delta^{1/2} + a_3\,\delta + a_4\,\delta^2 + a_5\,\delta^3 + a_6\,\delta^4. \tag{16}$$

The respective constants for $fs(\delta)$ and $h(\delta)$ are listed in Table IV.

Restricting the temperature range to $0.4 \leq T^* \leq 25$ and applying Eqs. (15) and (16) lead to a data reduction to yield 26 165 A_{00}^r and 27 579 A_{01}^r and A_{10}^r values. Because of the lack of A_{00}^r at $T^* < 1.3$ and $\rho^* > 0.3$ for fluids, 89 A_{00}^r values from Thol[24] were additionally considered (noting that the A_{00}^r fluid values in the supplement of Thol *et al.*[17] are incorrect and new values were therefore supplied by Thol[24]).

The results of the simulations are shown in Figs. 2(a)–2(c) as contour plots showing their magnitude. In the supplementary material, A_{00}^r, A_{01}^r, and A_{10}^r values, as well as the original p^* and U^* results of the simulations, are provided in the form of an *Excel*-spreadsheet. The respective errors σ_m are also included.

TABLE IV. Parameters for liquid δ' and vapor δ'' stability, the boiling curve pressure p_σ^*, the fluid/solid *MC*-separation line *fs*, and the limiting functions for the heterogeneous region *h*.

	$\delta'(\vartheta)$	$\delta''(\vartheta)$	$p_\sigma^*(T^*)$	$fs(\delta)$	$h(\delta)$
a_1	−0.256 866	−0.700 23	−5.356 53	−10.1899	0.270 714
a_2	14.041 6	−2.160 96	−1.931 12	29.9634	4.271 09
a_3	−46.300 0	−8.816 42	−17.264 8	−33.4296	−6.276 54
a_4	83.459 8	18.783 4	−18.902 2	15.3339	11.180 8
a_5	−74.636 0	−17.422	−151.893		−19.178 2
a_6	26.427 3	−1.713 87	147.669		10.201 8
a_7		−24.514	−468.657		

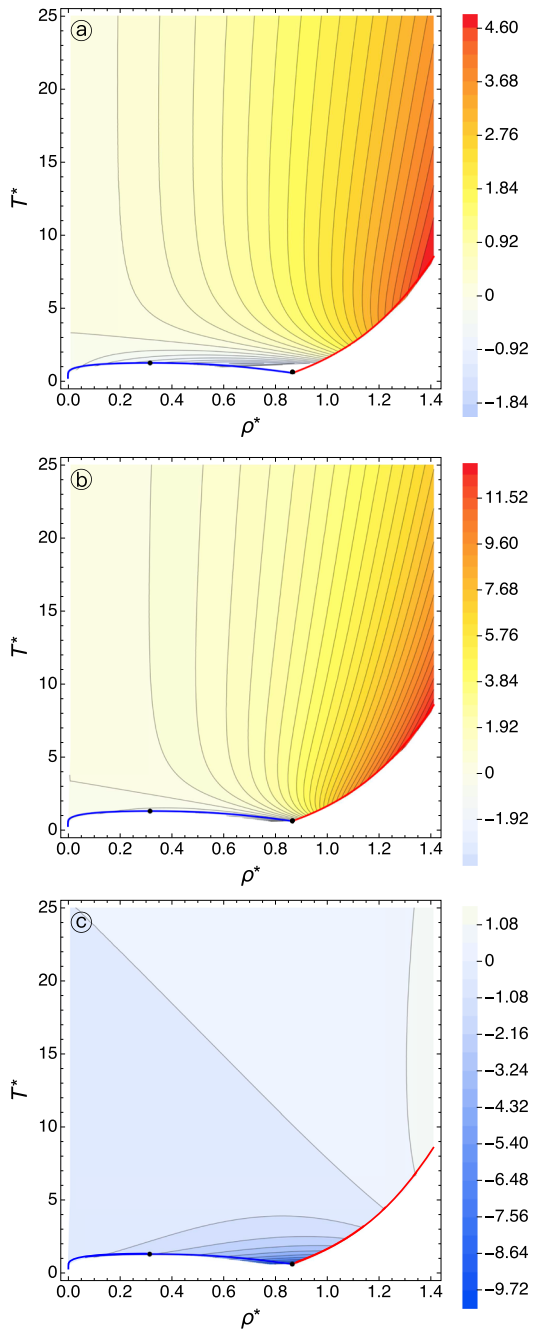

FIG. 2. Results of the *Monte Carlo* simulations: (a) A^r_{00}, (b) A^r_{01}, and (c) A^r_{10}. Contours are isolines of A^r_{mn}. Blue curve is the vapor/fluid phase field, and the red curve is the fluid/solid *MC*-separation line. Dots are the critical point and the intersection of the blue and red curve.

III. EQUATION OF STATE

The functional form chosen here for the residual part a^{r*} in the presented *EOS* uses a virial equation as a first approximation and differs therefore from the approach taken by Thol *et al.*[17]

The thermal virial equation a^{r*}_v is defined by

$$a^{r*}_v = \sum_{i=2}^{n} \frac{\delta^{i-1}}{i-1} B_i(\tau), \tag{17}$$

where B_i is a function of τ or T^* only. The virial equation is known to be an excellent approximation at low ρ^* and gets good predictions up to high T^*.[25] However, in the fluid (liquid) region at $\rho^* > 0.3$ and $T^* < 3$, the virial equation is known to be nonconvergent,[25] i.e., results from the virial equation are not suitable or acceptable at these conditions. The situation worsens exponentially with increasing order i of the thermal coefficients B_i. On the other hand, Thol *et al.*[17] uses successfully B_2, B_3, and B_4 as input for their *EOS* and reproduces the experimental virial coefficients as a function of T^*. Only B_3 shows minor deviations in the T^*-range of 0.3–3.0 demonstrating that the virial equation seems to be viable approximation for an *EOS* at higher T^*.

Here, the computationally known virial coefficients B_2–B_6 are used to formulate a preliminary *EOS* prior to any fitting to the *MC* results. For $B_{i\geq 7}$ from literature, the nonconvergence in the liquid region becomes too large to be corrected by a fit to a function with a reasonable amount of parameters (see below). However, as a first step, the parameters for thermal virial coefficients B_2–B_6 must be determined.

For B_2, an exact solution is available.[26–29] The solution can be formulated using a modified Bessel function[26] and the following form is valid:

$$B_2(\tau) = \frac{\sqrt{2}\pi^2}{3}\tau e^{\frac{\tau}{2}}\left(I_{-3/4}\left(\frac{\tau}{2}\right) - I_{-1/4}\left(\frac{\tau}{2}\right) - I_{1/4}\left(\frac{\tau}{2}\right) + I_{3/4}\left(\frac{\tau}{2}\right)\right). \tag{18}$$

The thermal virial coefficients B_3–B_6 are fitted to simulation data[30–38] using an equation presented by Feng *et al.*,[39]

$$B_i(\tau) = \left(\frac{1}{4\tau}\right)^{-\frac{i-1}{4}}\left(\tilde{B}^{SS}_i + \sum_{k=1}^{k_i} b_{i,k}\left(e^{c_i\sqrt{\tau}} - 1\right)^{\frac{2k-1}{4}}\right), \tag{19}$$

however, the exponent in sum-term is modified and the temperature dependence is formulated in τ. While Feng *et al.*[39] used integer values for the exponent, it has been observed that using an exponent in the form $(2k-1)/4$ leads to slightly higher R^2 values for B_5 and B_6 and such leads to lower residuals considering the same amount of parameters. In addition, the exponent $(2k-1)/4$ seems to be more adequate for the steep decrease of B_i at $T^* < 0.6$ and allows the calculation to low T^* down to approximately 0.25.

In total, 252, 433, 328, and 180 values are available for B_3–B_6, respectively. In the light of available data, the amount of parameters (13 for B_3–B_5 and 10 for B_6) seems to be of no consequence.

Dyer *et al.*[34] pointed out that error estimates for thermal virial coefficients in earlier literature were somewhat optimistic. This observation was not considered here, and all data were treated equal. No weighting scheme had been used, i.e., the errors of the individual values were not considered for fitting. Consequently, the derived values from the fits average existing values.

For the parameter $\tilde{B}^{SS}_n$, values are taken from Tan *et at.*[40] and Wheatley.[41] It is important to note that no *Monte Carlo* simulation data of the present communication are used for fitting of the parameters of B_3–B_6. The modeled τ-dependence is shown in Fig. 3, and the $\tilde{B}^{SS}_i$, $b_{i,k}$, and c_i coefficients are presented in Table V.

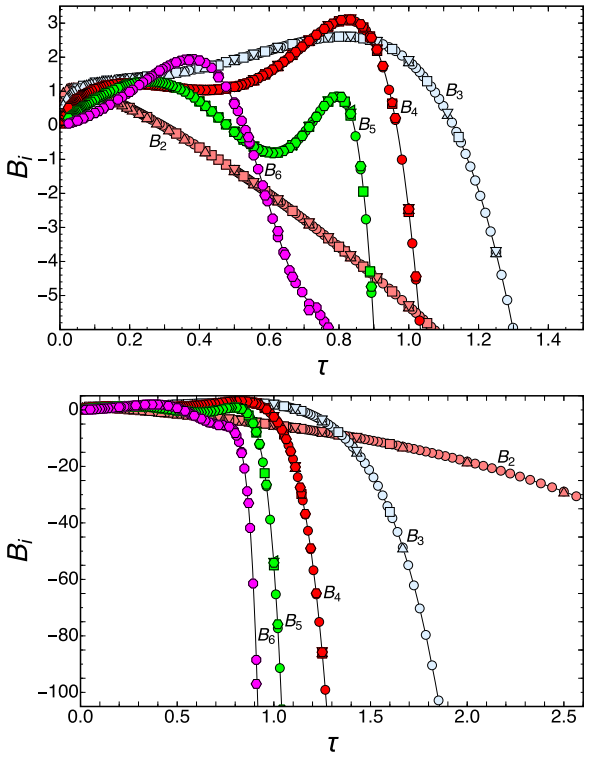

FIG. 3. Thermal virial coefficients B_2–B_6 as function of τ. The lower plot is an enlargement of the upper. [◯ (Ref. 33) △ (Ref. 38), ▽ (Ref. 36), ◁ (Ref. 32), □ (Ref. 30), ◇ (Ref. 31), ⬠ (Ref. 34), ⬡ (Ref. 35) ◯ (Ref. 37)].

The virial part (v) of the *EOS* is then

$$a_v^{r*} = \sum_{i=2}^{6} \frac{\delta^{i-1}}{i-1} B_i(\tau). \tag{20}$$

Figures 4(a)–4(c) show the difference of the *Monte Carlo* simulation results and the thermal virial coefficients $A^r_{mn} - A^{r\,v}_{mn}$ [for definitions of A^r_{mn} and $A^{r\,v}_{mn}$, see Eq. (8)]. It should be noted from Figs. 4(a) to 4(c) that except for the fluid field at low T^*, the virial part a_v^{r*} is a very good approximation to the simulation data.

The residual, the difference between $A^r_{mn} - A^{r\,v}_{mn}$, was then fitted using an equation analogous to Eq. (19),

$$C_i(\tau) = \left(\frac{1}{4\tau}\right)^{-\frac{i-1}{4}} \left(\tilde{C}_i^{SS} + \sum_{k=1}^{k_i} c_{i,k}\left(e^{d_i\sqrt{\tau}} - 1\right)^{\frac{2k-1}{4}}\right), \tag{21}$$

thereby the constants $\tilde{C}_n^{SS}$, $c_{n,k}$, and d_n have no physical significance, but mimic a similar dependence with respect to τ.

A^r_{00}, A^r_{01}, and A^r_{10} are used to fit the coefficients in Eq. (21). While A^r_{00} is derived from A^r_{01} according to the integral relationship [Eq. (14)] at constant T^*, the use of A^r_{00} is justified. The values of A^r_{00} include a set of A^r_{01}-values reflecting a set of different ρ^* at constant T^*. So, the fit of *EOS* not only uses the slopes A^r_{01} in respect to ρ^*, but also includes the functional values A^r_{00}.

No weighting scheme had been used for fitting. The derived coefficients are given in Table VI. Accordingly, the complete residual part of the derived *EOS* has then the following form:

$$a_v^{r*\,EOS} = \sum_{i=2}^{6} \frac{\delta^{i-1}}{i-1} B_i(\tau) + \sum_{i=7}^{16} \frac{\delta^{i-1}}{i-1} C_i(\tau). \tag{22}$$

The residuals $A^r_{mn} - A^{r\,EOS}_{mn}$ are presented in Figs. 5(a)–5(c). Magnification plots for the area $T^* \le 3$ are presented in the supplementary material (Figs. S1(a)–(c)) as well as formulations for the differentials A^o_{mn} and $A^{r\,EOS}_{mn}$ in respect of τ and δ up to $m, n = 3$. By comparing Figs. 4(a)–4(c) and 5(a)–5(c), it is observed that the situation in the liquid region is dramatically improved, but the high-T^* high-ρ^* region is only marginally better, showing also an opposite sign. This is an indication that more terms ($i > 16$) might be required for further improvement.

All fit procedures were performed using the *NonlinearModelFit* function of *Mathematica*.[42]

TABLE V. Parameters of the thermal virial coefficients.

	B_3	B_4
$\bar{B}_i^{SS}$	3.791 07	3.527 51
c_i	1.529 031 885	2.795 121 498
$b_{i,1}$	$1.221\,844\,737 \times 10^{-1}$	$-1.832\,133\,004 \times 10^{-2}$
$b_{i,2}$	−2.533 814 785	$-2.221\,029\,066 \times 10^{-1}$
$b_{i,3}$	2.321 052 047	−2.290 140 445
$b_{i,4}$	$-2.221\,116\,991 \times 10^{1}$	2.497 587 053
$b_{i,5}$	$6.037\,723\,605 \times 10^{1}$	−1.491 751 608
$b_{i,6}$	$-8.614\,627\,023 \times 10^{1}$	$5.194\,910\,488 \times 10^{-1}$
$b_{i,7}$	$7.947\,702\,893 \times 10^{1}$	$-7.580\,241\,786 \times 10^{-2}$
$b_{i,8}$	$-5.013\,039\,389 \times 10^{1}$	$-9.570\,910\,251 \times 10^{-3}$
$b_{i,9}$	$2.179\,355\,452 \times 10^{1}$	$6.444\,596\,963 \times 10^{-3}$
$b_{i,10}$	−6.423 839 356	$-1.323\,484\,892 \times 10^{-3}$
$b_{i,11}$	1.222 200 983	$1.400\,743\,960 \times 10^{-4}$
$b_{i,12}$	$-1.351\,435\,025 \times 10^{-1}$	$-7.861\,096\,502 \times 10^{-6}$
$b_{i,13}$	$6.519\,707\,093 \times 10^{-3}$	$1.749\,011\,555 \times 10^{-7}$
	B_5	B_6
$\bar{B}_i^{SS}$	2.114 94	0.769 53
c_i	4.903 830 267	5.539 252 062
$b_{i,1}$	$-5.737\,837\,739 \times 10^{-2}$	$-1.107\,146\,794 \times 10^{-1}$
$b_{i,2}$	$2.384\,059\,560 \times 10^{-1}$	$3.639\,967\,813 \times 10^{-1}$
$b_{i,3}$	$-3.175\,043\,752 \times 10^{-1}$	$-1.722\,555\,372 \times 10^{-1}$
$b_{i,4}$	$1.411\,210\,874 \times 10^{-1}$	$5.355\,823\,913 \times 10^{-2}$
$b_{i,5}$	$-4.065\,269\,634 \times 10^{-2}$	$-9.119\,290\,154 \times 10^{-3}$
$b_{i,6}$	$7.132\,4506\,69 \times 10^{-3}$	$6.312\,327\,708 \times 10^{-4}$
$b_{i,7}$	$-7.501\,879\,316 \times 10^{-4}$	$-6.471\,729\,317 \times 10^{-6}$
$b_{i,8}$	$5.000\,252\,419 \times 10^{-5}$	$-6.635\,662\,426 \times 10^{-7}$
$b_{i,9}$	$-2.224\,242\,683 \times 10^{-6}$	$1.145\,665\,574 \times 10^{-8}$
$b_{i,10}$	$6.334\,525\,666 \times 10^{-8}$	$-5.093\,701\,999 \times 10^{-10}$
$b_{i,11}$	$-1.124\,571\,857 \times 10^{-9}$	
$b_{i,12}$	$1.120\,406\,875 \times 10^{-11}$	
$b_{i,13}$	$-4.806\,632\,984 \times 10^{-14}$	

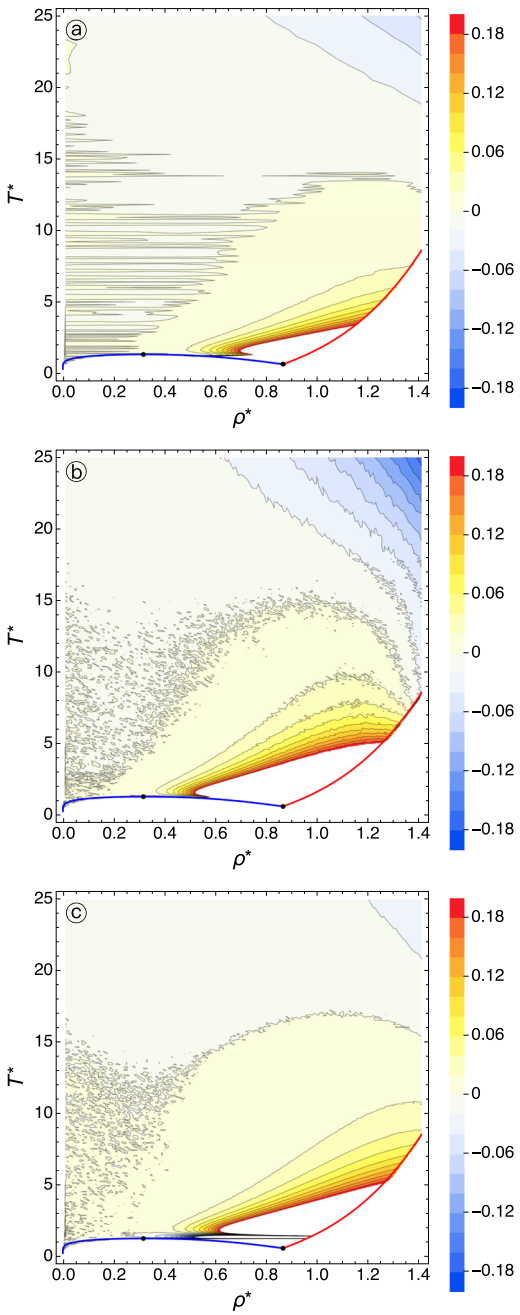

FIG. 4. Simulation after application of the thermal virial coefficients B_2–B_6: (a) $A^r_{00}-A^{r\,v}_{00}$, (b) $A^r_{01}-A^{r\,v}_{01}$, and (c) $A^r_{10}-A^{r\,v}_{10}$. Contours are isolines of $A^r_{mn}-A^{r\,v}_{mn}$. Legend for blue and red curves as well for dots as in Fig. 1. White areas designate a larger deviation as indicated by the side bar.

IV. CRITICAL POINT

The formal requirements for the critical point are

$$\left(\frac{\partial p^*}{\partial v^*}\right)_T = 0 \tag{23}$$

and

$$\left(\frac{\partial^2 p^*}{\partial v^{*2}}\right)_T = 0. \tag{24}$$

Using the definition of the pressure derivatives in Table I and (22) in conjunction with (23) and (24), the critical point is calculated to be $T^*_c = 1.3276$, $\rho^*_c = 0.3164$, and $p^*_c = 0.1356$. Table 10 in Thol *et al.*[17] reports various critical parameters for the *LJ* fluid collected from literature. The values found here are in good agreement with previous reported parameters. For instance, Thol *et al.*[17] used $T^*_c = 1.32$, $\rho^*_c = 0.31$, and $p^*_c = 0.1300$ as a prerequisite to derive their *EOS*. However, one should note that their resulting *EOS* yields $T^*_c = 1.3035$, $\rho^*_c = 0.3104$, and $p^*_c = 0.1212$ when Eqs. (23) and (24) are applied.

V. LIQUID-VAPOR PHASE FIELD

The requirements for the vapor-liquid equilibrium are that both phases have the same pressure p^*_σ and temperature T^*_σ and that the *fugacity coefficient* ϕ for each phase is equal ($'$ liquid, $''$ vapor),

$$\phi'(\delta',\tau) = \phi''(\delta'',\tau). \tag{25}$$

This leads to the following equilibrium conditions (see also equations in Table I):

$$\frac{\delta'}{\delta''} = \frac{(1+A^r_{01}(\delta'',\tau))}{(1+A^r_{01}(\delta',\tau))} \tag{26}$$

and

$$(1+A^r_{01}(\delta',\tau))\left(\frac{\delta'}{\delta''}-1\right)-\ln\left(\frac{\delta'}{\delta''}\right) = A^r_{00}(\delta',\tau)-A^r_{00}(\delta'',\tau). \tag{27}$$

The positions of the respective phase equilibria are fitted using the following relation:

$$\vartheta = 1-\frac{T^*}{T^*_c}. \tag{28}$$

The density of the vapor phase δ'' as a function of ϑ at the phase boundary becomes

$$\ln\left(\frac{\delta''}{\delta_c}\right) = a_1\vartheta^{1/3}+a_2\vartheta^{2/3}+a_3\vartheta^{3/3}+a_4\vartheta^{4/3} + a_5\vartheta^{5/3}+a_6\vartheta^{6/3}+a_7\vartheta^{15/3} \tag{29}$$

and that for the liquid phase δ'

$$\frac{\delta'}{\delta_c} = 1+a_1\vartheta^{1/3}+a_2\vartheta^{2/3}+a_3\vartheta^{3/3}+a_4\vartheta^{4/3}+a_5\vartheta^{5/3}+a_6\vartheta^{6/3}. \tag{30}$$

The pressure at the phase equilibrium p^*_σ is

$$\ln\left(\frac{p^*_\sigma}{p^*_c}\right) = \frac{T^*}{T^*_c}\left(a_1\vartheta+a_2\vartheta^{3/2}+a_3\vartheta^{5/2}+a_4\vartheta^{7/2} + a_5\vartheta^{6}+a_6\vartheta^{15/2}+a_7\vartheta^{19/2}\right). \tag{31}$$

The coefficients for all 3 functions are listed in Table IV using $T^*_c = 1.3276$, $\rho^*_c = \delta_c = 0.3164$, and $p^*_c = 0.1356$. Table VII compares the densities δ', δ'', and pressure p^*_σ at the liquid-vapor phase

TABLE VI. Fit parameters for Eq. (21).

	C_7	C_8	C_9	C_{10}	C_{11}
$\tilde{C}_i^{SS}$	$2.356\,773\,117 \times 10^{3}$	$-3.264\,039\,611 \times 10^{3}$	$-7.804\,186\,018 \times 10^{4}$	$4.734\,725\,795 \times 10^{5}$	$-1.317\,864\,191 \times 10^{6}$
d_i	4.85	4.85	4.85	4.85	4.85
$c_{i,1}$	$-3.848\,657\,712 \times 10^{3}$	$1.214\,533\,953 \times 10^{4}$	$5.841\,998\,321 \times 10^{4}$	$-4.717\,257\,385 \times 10^{5}$	$1.411\,244\,301 \times 10^{6}$
$c_{i,2}$	$1.940\,790\,808 \times 10^{3}$	$-9.125\,315\,944 \times 10^{3}$	$5.336\,019\,753 \times 10^{3}$	$7.338\,796\,875 \times 10^{4}$	$-2.875\,424\,926 \times 10^{5}$
$c_{i,3}$	$-6.786\,775\,725 \times 10^{2}$	$3.397\,150\,517 \times 10^{3}$	$-6.393\,577\,02 \times 10^{3}$	$1.526\,191\,655 \times 10^{3}$	$2.109\,845\,310 \times 10^{4}$
$c_{i,4}$	$1.592\,726\,729 \times 10^{2}$	$-7.355\,400\,823 \times 10^{2}$	$1.371\,420\,01 \times 10^{3}$	$-1.479\,809\,349 \times 10^{3}$	$9.648\,092\,327 \times 10^{2}$
$c_{i,5}$	$-2.733\,389\,532 \times 10^{1}$	$1.207\,984\,183 \times 10^{2}$	$-1.843\,597\,578 \times 10^{2}$	$1.033\,775\,279 \times 10^{2}$	$-1.118\,483\,146 \times 10^{1}$
$c_{i,6}$	3.305 728 801	$-1.595\,650\,007 \times 10^{1}$	$2.756\,765\,411 \times 10^{1}$	$-1.762\,232\,710 \times 10^{1}$	−5.953 997 923
$c_{i,7}$	$-2.396\,300\,005 \times 10^{-1}$	1.301 737 514	−2.765 120 060	3.029 682 621	−1.736 288 154
$c_{i,8}$	$8.107\,532\,579 \times 10^{-3}$	$-4.828\,021\,321 \times 10^{-2}$	$1.107\,783\,436 \times 10^{-1}$	$-1.382\,464\,464 \times 10^{-1}$	$1.102\,848\,617 \times 10^{-1}$
$c_{i,9}$	$-5.209\,209\,916 \times 10^{-5}$	$4.779\,918\,832 \times 10^{-4}$	$-1.100\,471\,432 \times 10^{-3}$	$1.049\,186\,458 \times 10^{-3}$	$-4.233\,596\,547 \times 10^{-4}$
$c_{i,10}$	$-1.863\,883\,724 \times 10^{-6}$	$4.808\,860\,997 \times 10^{-6}$	$-4.538\,508\,711 \times 10^{-6}$	$1.455\,012\,606 \times 10^{-6}$	
$c_{i,11}$	$6.787\,957\,968 \times 10^{-9}$	$-3.433\,240\,822 \times 10^{-9}$			

	C_{12}	C_{13}	C_{14}	C_{15}	C_{16}
$\tilde{C}_i^{SS}$	$2.146\,863\,058 \times 10^{6}$	$-2.165\,267\,779 \times 10^{6}$	$1.335\,386\,749 \times 10^{6}$	$-4.628\,739\,042 \times 10^{5}$	$6.922\,915\,835 \times 10^{4}$
d_i	4.85	4.85	4.85	4.85	4.85
$c_{i,1}$	$-2.385\,034\,755 \times 10^{6}$	$2.465\,995\,272 \times 10^{6}$	$-1.550\,792\,557 \times 10^{6}$	$5.466\,032\,853 \times 10^{5}$	$-8.300\,129\,372 \times 10^{4}$
$c_{i,2}$	$5.411\,774\,951 \times 10^{5}$	$-5.990\,022\,139 \times 10^{5}$	$3.971\,186\,192 \times 10^{5}$	$-1.464\,740\,110 \times 10^{5}$	$2.318\,027\,845 \times 10^{4}$
$c_{i,3}$	$-5.532\,941\,146 \times 10^{4}$	$7.174\,967\,760 \times 10^{4}$	$-5.317\,159\,494 \times 10^{4}$	$2.148\,725\,004 \times 10^{4}$	$-3.684\,215\,524 \times 10^{3}$
$c_{i,4}$	$2.842\,688\,756 \times 10^{2}$	$-1.763\,990\,307 \times 10^{3}$	$2.096\,231\,490 \times 10^{3}$	$-1.141\,346\,457 \times 10^{3}$	$2.443\,351\,261 \times 10^{2}$
$c_{i,5}$	$5.210\,586\,49 \times 10^{1}$	$-1.121\,805\,527 \times 10^{2}$	$7.436\,426\,163 \times 10^{1}$	$-1.333\,984\,225 \times 10^{1}$	−2.185 586 771
$c_{i,6}$	$1.569\,383\,441 \times 10^{1}$	−7.327 702 248	−1.053 356 075	1.604 683 226	$-2.645\,512\,917 \times 10^{-1}$
$c_{i,7}$	$2.519\,375\,463 \times 10^{-1}$	$3.057\,812\,577 \times 10^{-1}$	$-1.621\,886\,602 \times 10^{-1}$	$1.067\,758\,340 \times 10^{-2}$	$3.982\,533\,293 \times 10^{-3}$
$c_{i,8}$	$-5.923\,068\,772 \times 10^{-2}$	$1.906\,868\,401 \times 10^{-2}$	$-2.542\,729\,177 \times 10^{-3}$		
$c_{i,9}$	$5.305\,829\,584 \times 10^{-5}$				

field to the results of Thol *et al.*[17] Below $T^* \leq 1.1$, respective densities are quite similar, but for $T^* > 1.1$, when approaching T_c^*, larger deviations are observed.

In Figs. 6(a) and 6(b), the behavior of A_{00}^r within the two-phase field is shown for the *EOS* presented here and that of Thol *et al.*[17] It can be seen in Fig. 6(b) that there is a significant depression below the critical point in Thol *et al.*,[17] which is due to the use of Gaussian bell-shaped functions. Such Gaussian bell-shaped functions are "patches" to certain ρ^*–T^* regions. However, such holes are physically not justified. In principal, those "patches" in the two phase field do not affect any calculations of A_{00}^* in one phase region. However, if calculations are performed in two phase region, this might also affect any chemical equilibrium considerations when accidentally touched. The presented *EOS* [Fig. 6(a)] shows a sharp cliff in the liquid/vapor region for $T^* < 0.8$. It is unclear if this is physically justified or a relic of the virial approach used here.

VI. EXTRAPOLATION AND COMPARISON

The *EOS* was fitted to data with $T^* \leq 25$ and $\rho^* \leq 1.41$. Some simulation results at extreme conditions[43–45] are available in the literature. In Table VIII, A_{10}^r and A_{01}^r values for $T^* > 30$ are compared with these literature results and the percentage of deviation is given. The deviation is in most cases well below 4% for A_{10}^r and well below 3% for A_{01}^r. It rarely exceeds 5%. The highest deviation for A_{10}^r with −11.36% is at $\rho^* = 0.2$ and $T^* = 100$. However, here the absolute deviation from simulation of A_{10}^r is only 0.004. Even at very extreme conditions ($T^* > 130$ or $\rho^* > 2$), the deviations from the *EOS* are well below 5%. This extrapolation behavior can be attributed to the good approximation of the application of the virial equation up to the order of $i = 6$.

Figures 7(a) and 7(b) show the behavior of the *EOS* at low ρ^* at 0.01–0.10 and $T^* \leq 10$ for A_{01}^r and A_{10}^r in respect to the simulation data. In this region, the simulation errors for A_{01}^r and A_{10}^r are in the order of $1–2 \times 10^{-4}$. The deviations of the *EOS* to the calculations are in the order of 2σ of the simulation errors. The observed deviation are just the noise of the simulations.

The presented *EOS* compares favorably with the *EOS* of Thol *et al.*[17] in the region ρ^*–T^* space for which their *EOS* is valid [Figs. S2(a)–(d) in the supplementary material]. If compared to the absolute values of the simulations in Figs. 2(a)–2(c), the deviations for A_{00}^r, A_{01}^r, and A_{10}^r are mostly minor. However, at $T^* < 1.5$ and $\rho^* < 0.4$, around the critical point, larger deviations are observed.

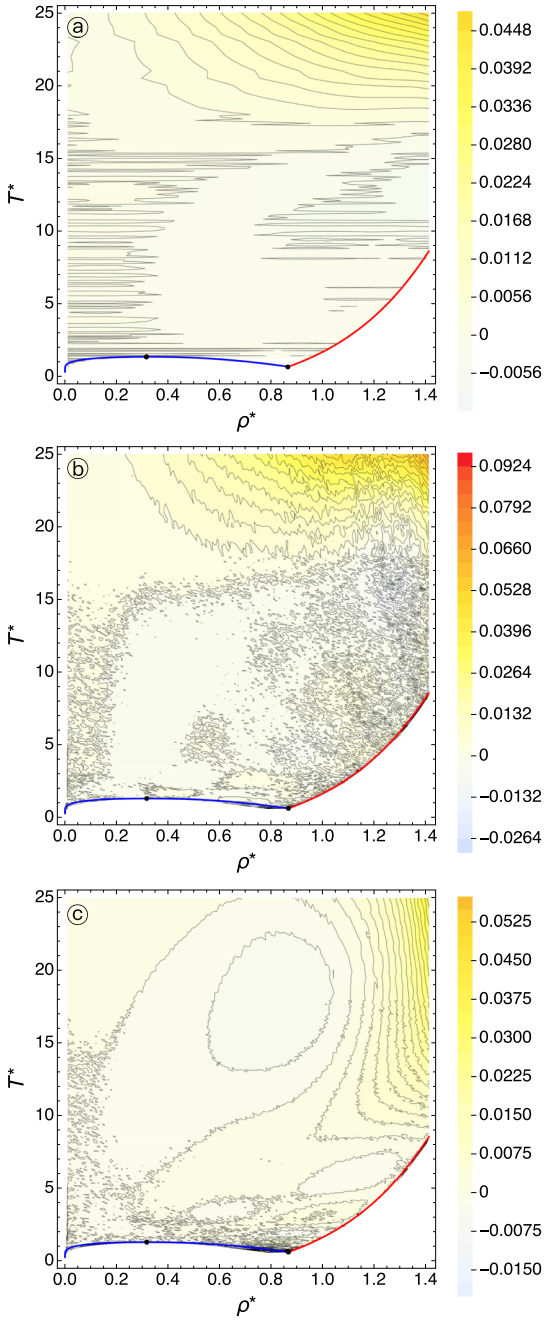

FIG. 5. Residuals for the *EOS*: (a) $A^r_{00} - A^{r\,EOS}_{00}$, (b) $A^r_{01} - A^{r\,EOS}_{01}$, and (c) $A^r_{10} - A^{r\,EOS}_{10}$. Contours are isolines of $A^r_{mn} - A^{r\,EOS}_{mn}$. In the case of $A^r_{00} - A^{r\,EOS}_{00}$, only very few A^r_{00}-values from Thol *et al.*[17] for $T^* < 1$ are available and ρ^* does not exceed 0.87. So, isolines could not be calculated and this region is left white. Legend for blue and red curves as well as for dots as in Fig. 1.

The reason for this is the functional form (Gaussian bell-shaped functions) used by Thol *et al.*,[17] which leads to the "hole" described in Fig. 6(b). The influence on derivatives of the Gaussian bell-shaped functions is severe and may affect the values of A^r_{mn} considerably

TABLE VII. Densities at the liquid-vapor phase field. For *EOS* presented here, p^*_σ-, δ'-, and δ''-values are calculated directly from (26) and (27) and not via (29) and (30).

	EOS			Thol *et al.*[17]		
T^*	p^*_σ	δ''	δ'	p^*_σ	δ''	δ'
0.7	0.001 36	0.001 98	0.842 75	0.001 37	0.001 99	0.842 60
0.8	0.004 63	0.006 07	0.799 60	0.004 64	0.006 08	0.799 18
0.9	0.011 80	0.014 44	0.753 27	0.011 82	0.014 47	0.752 00
1.0	0.024 85	0.029 40	0.702 26	0.024 90	0.029 45	0.701 85
1.1	0.045 86	0.054 77	0.642 29	0.045 91	0.054 74	0.642 06
1.2	0.076 92	0.098 98	0.566 78	0.076 86	0.097 92	0.565 70
1.3	0.120 77	0.199 72	0.442 71	0.119 79	0.192 32	0.435 72

having numerous minima and maxima over a quite large ρ^*–T^* range. Only 1 of the 11 bell functions used by Thol *et al.*[17] leads to such drastic depression of A^r_{00}, but numerous extrema can be observed for A^r_{01}, A^r_{10}, and A^r_{20} in the liquid region [Figs. S2(b)–(d)

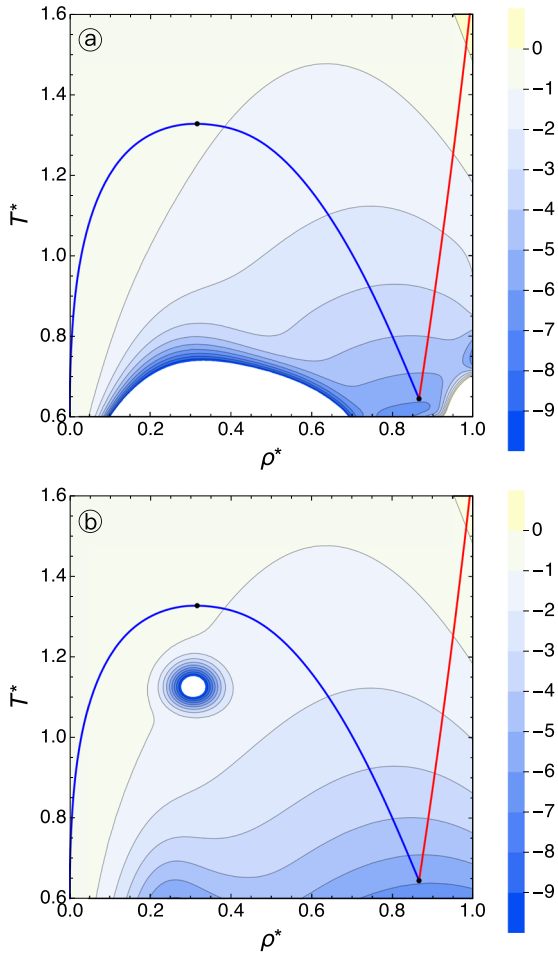

FIG. 6. A^r_{00} within the 2 phase field: (a) *EOS* and (b) Thol *et al.*[17] Contours are isolines of A^r_{00}. Legend for blue and red curves as well as for dots as in Fig. 1.

TABLE VIII. Extrapolation from data by Miyano,[45] Shaw,[44] Hansen[43] and deviation to the simulation presented in this study.

ρ^*	T^*	A_{10}^r	$A_{10}^{r\,EOS}$	%Δ	A_{01}^r	$A_{01}^{r\,EOS}$	%Δ
0.2	50	0.0300	0.0284	−6.37	0.2400	0.2492	3.73
0.4	50	0.0700	0.0732	4.52	0.5800	0.5908	1.86
0.6	50	0.1400	0.1416	1.25	1.0400	1.0604	1.94
0.8	50	0.2500	0.2416	−3.47	1.6800	1.6924	0.74
1.0	50	0.4000	0.3860	−3.62	2.5100	2.5340	0.95
0.2	100	0.0400	0.0360	−11.36	0.2200	0.2220	0.82
0.4	100	0.0800	0.0856	6.46	0.5000	0.5112	2.16
0.6	100	0.1500	0.1532	2.18	0.8800	0.8920	1.37
0.8	100	0.2400	0.2432	1.34	1.3500	1.3852	2.55
1.0	100	0.3600	0.3604	0.08	1.9700	2.0092	1.95
Shaw[44]							
0.864	30.886	0.2580	0.2604	0.88	2.1796	2.2352	2.50
0.864	33.461	0.2628	0.2660	1.22	2.1212	2.1828	2.84
1.2	34.840	0.6508	0.6268	−3.84	4.2648	4.2032	−1.46
1.2	39.596	0.6388	0.6144	−3.99	4.0396	3.9880	−1.30
1.2	44.633	0.6260	0.6020	−3.96	3.8392	3.8000	−1.04
1.2	49.946	0.6124	0.5904	−3.78	3.6600	3.6336	−0.72
1.2	55.533	0.5992	0.5788	−3.51	3.4980	3.4856	−0.36
1.2	61.386	0.5856	0.5676	−3.17	3.3516	3.3528	0.04
1.2	66.806	0.5740	0.5580	−2.83	3.2328	3.2456	0.40
1.2	73.142	0.5612	0.5480	−2.41	3.1104	3.1356	0.80
1.2	78.978	0.5500	0.5392	−2.03	3.0104	3.0456	1.16
1.2	84.998	0.5396	0.5308	−1.65	2.9180	2.9628	1.52
1.2	91.197	0.5296	0.5228	−1.28	2.8324	2.8860	1.86
1.2	97.567	0.5200	0.5152	−0.91	2.7532	2.8144	2.18
1.2	104.100	0.5108	0.5080	−0.56	2.6792	2.7476	2.49
1.2	110.790	0.5020	0.5008	−0.22	2.6108	2.6856	2.78
1.2	117.630	0.4936	0.4940	0.10	2.5468	2.6272	3.06
1.2	124.612	0.4856	0.4876	0.39	2.4872	2.5724	3.31
1.2	130.835	0.4788	0.4820	0.64	2.4384	2.5272	3.52
1.2	136.249	0.4736	0.4776	0.83	2.3984	2.4900	3.68
Hansen[43]							
0.2	100	0.0360	0.0360	−0.22	0.2212	0.2220	0.37
0.4	100	0.0852	0.0856	0.61	0.5048	0.5112	1.18
0.5	100	0.1152	0.1168	1.62	0.6752	0.6888	1.98
0.666	100	0.1752	0.1804	2.99	1.0072	1.0416	3.34
1.0	100	0.3608	0.3604	−0.19	1.9500	2.0092	2.95
1.33	100	0.6480	0.6332	−2.35	3.3600	3.3848	0.73
1.4	100	0.7340	0.7056	−4.01	3.7600	3.7340	−0.70
2.0	100	1.7672	1.6912	−4.49	8.5000	7.9824	−6.48
2.22	100	2.3460	2.3796	1.41	11.1000	10.8560	−2.25
2.38	100	2.8872	3.0164	4.28	13.4600	13.5900	0.96
2.5	100	3.3040	3.4824	5.12	15.2900	15.6500	2.30

in the supplementary material], which are due to the other 10 bell functions.

Percent assessments of any errors like in Thol *et al.*[17] are avoided here because values of A_{00}^r, A_{01}^r, and A_{10}^r change sign as a function of ρ^*–T^*, leading to infinity deviations in these regions.

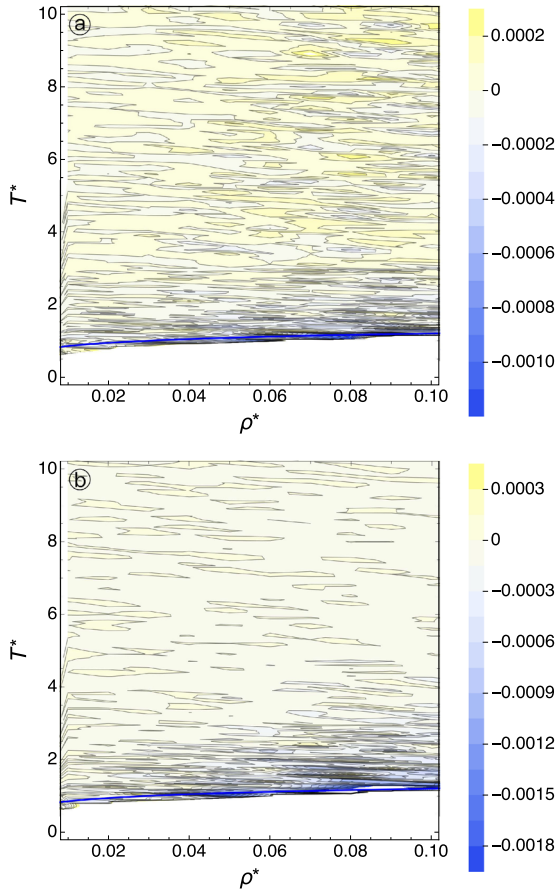

FIG. 7. Residuals for the *EOS* at low ρ^*: (a) $A_{01}^r - A_{01}^{r\,EOS}$ and (b) $A_{10}^r - A_{10}^{r\,EOS}$. At the shown conditions, the residuals are basically the noise of the simulation. Contours are isolines of $A_{mn}^r - A_{mn}^{r\,EOS}$. Legend for blue line as in Fig. 1.

VII. CONCLUSION

Based on the thermal virial equation up to the order $B_{i\leq 6}$, an *EOS* for the *LJ* fluid was formulated. The required thermal virial coefficients are fitted to simulations available in the literature. The nonconvergent behavior of the thermal virial equation in the liquid region is compensated by fitting correction functions to a large set of *Monte Carlo* simulations over a large density and temperature range ($0.002 < \rho^* < 1.41$, $0.4 < T^* < 25$). These functions have the same mathematical form as the thermal virial coefficients, but are only empirical correction terms. Gaussian bell-shaped functions are completely avoided. In addition, the dependency on ρ^* and T^* of the *EOS* is strictly separated due to the virial approach. The EOS can be extrapolated to extreme conditions (at least, $\rho^* < 2.5$, $T^* < 140$). In the heterogeneous region (*MC* yielding more than 1 phase) of the liquid-vapor phase field, the EOS seems to be accessible above $T^* > 0.8$.

SUPPLEMENTARY MATERIAL

The supplementary material contains Figs. S1(a)–(c) and S2(a)–(d), the formulation of A_{00}^o and A_{00}^r, and their respective

derivatives A^o_{mn} and A^r_{mn} ($m \leq 3$ and $n \leq 3$) for use in Eq. (8), the required implementation of the modified Bessel function used in Eq. (18), and an *Excel* spreadsheet containing the *MC*-results including errors for U^*, p^*, and T^*_{config} as well as thereof the resulting values of A^r_{00}, A^r_{01}, and A^r_{10} and their respective errors.

The supplementary material also contains code for the residual part of the *EOS* and their derivatives in *C* and C^{++} as a function or a class, respectively, and as well as a *Mathematica* package.

Table S1 provides numerical values for A^r_{00}, A^r_{10}, A^r_{20}, A^r_{01}, A^r_{11}, A^r_{21}, A^r_{02}, A^r_{12}, and A^r_{22}, which can be used for the verification of computer codes.

ACKNOWLEDGMENTS

I am thankful to Ilias Efthymiopoulos, Dennis Gottschalk, Monika Koch-Müller, Sergey Lobanov, Maribel Núñez Valdez, Hans Josef Reichmann, Melanie Sieber, Sergio Speziale, and Johannes Wagner for constructive discussions. The remarks of an unknown reviewer were especially of great help to improve the manuscript considerably.

REFERENCES

[1] S. Churakov and M. Gottschalk, "Perturbation theory based equation of state for polar molecular fluids: I. Pure fluids," Geochim. Cosmochim. Acta **67**, 2397–2414 (2003).
[2] S. Churakov and M. Gottschalk, "Perturbation theory based equation of state for polar molecular fluids: II. Fluid mixtures," Geochim. Cosmochim. Acta **67**, 2415–2425 (2003).
[3] C. Twu, K. Gubbins, and C. Gray, "Excess thermodynamic properties for liquid mixtures of non-spherical molecules," Mol. Phys. **29**, 713–729 (1975).
[4] C. H. Twu, K. E. Gubbins, and C. G. Gray, "Thermodynamics of mixtures of nonspherical molecules. III. Fluid phase equilibria and critical loci," J. Chem. Phys. **64**, 5186–5197 (1976).
[5] C. G. Gray, K. E. Gubbins, and C. H. Twu, "Perturbation theory for molecular fluids: Third-order term in the Pople expansion," J. Chem. Phys. **69**, 182–193 (1978).
[6] C. Twu and K. Gubbins, "Thermodynamics of polyatomic fluid mixtures—II: Polar, quadrupolar and octopolar molecules," Chem. Eng. Sci. **33**, 879–887 (1978).
[7] K. Gubbins and C. Twu, "Thermodynamics of polyatomic fluid mixtures—I theory," Chem. Eng. Sci. **33**, 863–878 (1978).
[8] K. Lucas, *Applied Statistical Thermodynamics* (Springer Berlin Heidelberg, 1991).
[9] J. E. Jones, "On the determination of molecular fields. II. From the equation of state of a gas," Proc. R. Soc. London, Ser. A **106**, 463–477 (1924).
[10] G. Mie, "Zur kinetischen theorie der einatomigen Körper," Ann. Phys. **316**, 657–697 (1903).
[11] J. K. Johnson, J. A. Zollweg, and K. E. Gubbins, "The Lennard-Jones equation of state revisited," Mol. Phys. **78**, 591–618 (1993).
[12] J. Kolafa and I. Nezbeda, "The Lennard-Jones fluid: An accurate analytic and theoretically-based equation of state," Fluid Phase Equilib. **100**, 1–34 (1994).
[13] M. Mecke, A. Müller, J. Winkelmann, J. Vrabec, J. Fischer, R. Span, and W. Wagner, "An accurate Van der Waals-type equation of state for the Lennard-Jones fluid," Int. J. Thermophys. **17**, 391–404 (1996).
[14] M. Mecke, A. Müller, J. Winkelmann, J. Vrabec, J. Fischer, R. Span, and W. Wagner, "Errata," Int. J. Thermophys. **19**, 1493–1498 (1998).
[15] H.-O. May and P. Mausbach, "Riemannian geometry study of vapor-liquid phase equilibria and supercritical behavior of the Lennard-Jones fluid," Phys. Rev. E **85**, 031201 (2012).
[16] H.-O. May and P. Mausbach, "Erratum: Riemannian geometry study of vapor-liquid phase equilibria and supercritical behavior of the Lennard-Jones fluid [Phys. Rev. E 85, 031201 (2012)]," Phys. Rev. E **86**, 059905 (2012).
[17] M. Thol, G. Rutkai, A. Köster, R. Lustig, R. Span, and J. Vrabec, "Equation of state for the Lennard-Jones fluid," J. Phys. Chem. Ref. Data **45**, 023101 (2016).
[18] R. Lustig, "Statistical thermodynamics in the classical molecular dynamics ensemble. I. Fundamentals," J. Chem. Phys. **100**, 3048–3059 (1994).
[19] R. Lustig, "Statistical thermodynamics in the classical molecular dynamics ensemble. II. Application to computer simulation," J. Chem. Phys. **100**, 3060–3067 (1994).
[20] R. Lustig, "Statistical thermodynamics in the classical molecular dynamics ensemble. III. Numerical results," J. Chem. Phys. **100**, 3068–3078 (1994).
[21] R. Lustig, "Microcanonical Monte Carlo simulation of thermodynamic properties," J. Chem. Phys. **109**, 8816–8828 (1998).
[22] G. Rutkai, M. Thol, R. Lustig, R. Span, and J. Vrabec, "Communication: Fundamental equation of state correlation with hybrid data sets," J. Chem. Phys. **139**, 041102 (2013).
[23] M. P. Allen and D. J. Tildesley, *Computer Simulation of Liquids*, 2nd ed. (Oxford University Press, Oxford, United Kingdom, 2017), ISBN: 978-0-19-252470-6.
[24] M. Thol, personal communication (2019).
[25] A. J. Schultz and D. A. Kofke, "Vapor-phase metastability and condensation via the virial equation of state with extrapolated coefficients," Fluid Phase Equilib. **409**, 12–18 (2016).
[26] P. Vargas, E. Munoz, and L. Rodriguez, "Second virial coefficient for the Lennard-Jones potential," Physica A **290**, 92–100 (2001).
[27] M. L. Glasser, "Second virial coefficient for a Lennard-Jones (2n-n) system in d dimensions and confined to a nanotube surface," Phys. Lett. A **300**, 381–384 (2002).
[28] A. González-Calderón and A. Rocha-Ichante, "Second virial coefficient of a generalized Lennard-Jones potential," J. Chem. Phys. **142**, 034305 (2015).
[29] R. J. Sadus, "Intermolecular potential-based equations of state from molecular simulation and second virial coefficient properties," J. Phys. Chem. B **122**, 7757–7763 (2018).
[30] J. A. Barker, P. J. Leonard, and P. Pompe, "Fifth virial coefficients," J. Chem. Phys. **44**, 4206–4211 (1966).
[31] D. Henderson and L. Oden, "Virial expansion for the radial distribution function of a fluid using the 6:12 potential," Mol. Phys. **10**, 405–425 (1966).
[32] S. Kim, D. Henderson, and L. Oden, "Exact values for the pair distribution function and direct correlation function of a 6:12 fluid at low densities," Trans. Faraday Soc. **65**, 2308–2319 (1969).
[33] T. F. Sun and A. S. Teja, "An equation of state for real fluids based on the Lennard-Jones potential," J. Phys. Chem. **100**, 17365–17372 (1996).
[34] K. M. Dyer, J. S. Perkyns, and B. M. Pettitt, "A reexamination of virial coefficients of the Lennard-Jones fluid," Theor. Chem. Acc. **105**, 244–251 (2001).
[35] A. J. Schultz and D. A. Kofke, "Sixth, seventh and eighth virial coefficients of the Lennard-Jones model," Mol. Phys. **107**, 2309–2318 (2009).
[36] K. R. S. Shaul, A. J. Schultz, and D. A. Kofke, "The effect of truncation and shift on virial coefficients of Lennard-Jones potentials," Collect. Czech. Chem. Commun. **75**, 447–462 (2010).
[37] A. J. Schultz, N. S. Barlow, V. Chaudhary, and D. A. Kofke, "Mayer sampling Monte Carlo calculation of virial coefficients on graphics processors," Mol. Phys. **111**, 535–543 (2013).
[38] R. J. Wheatley, personal communication (2019).
[39] C. Feng, A. J. Schultz, V. Chaudhary, and D. A. Kofke, "Eighth to sixteenth virial coefficients of the Lennard-Jones model," J. Chem. Phys. **143**, 044504 (2015).
[40] T. Tan, A. J. Schultz, and D. A. Kofke, "Virial coefficients, equation of state, and solid–fluid coexistence for the soft sphere model," Mol. Phys. **109**, 123–132 (2011).
[41] R. J. Wheatley, "Calculation of high-order virial coefficients with applications to hard and soft spheres," Phys. Rev. Lett. **110**, 200601 (2013).
[42] Wolfram Research, Inc., Mathematica, Version 12.0, 2019.
[43] J.-P. Hansen, "Phase transition of the Lennard-Jones system. II. High-temperature limit," Phys. Rev. A **2**, 221–230 (1970).
[44] M. S. Shaw, "A density of states transformation Monte Carlo method: Thermodynamics of the Lennard-Jones fluid," J. Chem. Phys. **89**, 2312–2323 (1988).
[45] Y. Miyano, "An equation of state for Lennard-Jones pure fluids applicable over a very wide temperature range," Fluid Phase Equilib. **85**, 71–80 (1993).